coatings

MDPI

Article

Novel Polyoxovanadate and Its Phase Transition Product for Electrochemical Performance of Aqueous Zinc-Ion Batteries

Wang Cai [1], Fengqiao Chen [2], Yue Zhao [1], Lu Jin [1,3,*] and Guoying Wei [1,*]

[1] College of Materials and Chemistry, China Jiliang University, Hangzhou 310018, China
[2] Hangzhou Electric Power Design Institute Co., Ltd., No. 388 Shaoxing Road, Hangzhou 310015, China
[3] Fujian Provincial Key Laboratory of Advanced Inorganic Oxygenated Materials, College of Chemistry, Fuzhou University, Fuzhou 350108, China
* Correspondence: lujin@cjlu.edu.cn (L.J.); guoyingwei@cjlu.edu.cn (G.W.)

Abstract

As an innovative technique in the field of energy storage, aqueous zinc-ion batteries (AZIBs) have garnered considerable research interest over recent years. However, designing and developing high-performance cathode materials for AZIBs remains a primary challenge. In this study, a novel POV-based cathode material, $[KV_{16}O_{38}]_2[Zn_2(en)_5][Zn(en)_2H_2O]_4{\cdot}en{\cdot}12H_2O{\cdot}6OH^-$ (KZVO), was first synthesized using a hydrothermal method, demonstrating a high specific capacity of 255.9 mAh g^{-1} at 0.5 A g^{-1} and excellent long-term cycling performance, retaining 206.5 mAh g^{-1} after 2000 cycles at 4 A g^{-1}, with a capacity retention of 77.6%. It is noteworthy that KZVO undergoes a gradual phase transition during electrochemical cycling. At 4 A g^{-1}, the phase transformation is completed after approximately 580 cycles, and the newly formed phase remains stable during subsequent cycles. Additionally, ex situ XRD and XPS analyses were conducted to further investigate the phase evolution and Zn^{2+} storage mechanism. In summary, this work not only demonstrates the effective utilization of POV-based cathode materials but also provides a novel perspective for the design of future AZIB cathode materials.

Keywords: aqueous zinc-ion batteries; cathode materials; polyoxovanadates; crystal structure; electrochemical performance; phase transition product

1. Introduction

With the sustained growth in the global demand for energy and the progressive depletion of fossil fuel resources, the energy crisis and environmental issues have become major challenges facing human society [1–4]. The advancement of sustainable and energy-efficient systems, particularly efficient energy storage technologies, is of great importance for promoting the energy transition, reducing carbon emissions, and addressing climate change [5–8]. Aqueous zinc-ion batteries (AZIBs), which utilize aqueous electrolytes, offer higher safety, better environmental compatibility, and greater cost-effectiveness [9–11]. Furthermore, zinc metal employed as the anode material delivers a high theoretical capacity of 820 mAh g^{-1} and a low redox potential of −0.76 V relative to the standard hydrogen electrode (SHE). However, the practical performance of AZIBs remains constrained by the cathode materials [12,13]. At present, AZIB cathode materials typically experience capacity fading, structural instability, and limited cycling life, which severely hinder their commercial application. Accordingly, the exploration and rational design of

Check for updates

Academic Editor: Octavian Buiu

Received: 27 April 2026
Revised: 13 May 2026
Accepted: 14 May 2026
Published: 17 May 2026

Copyright: © 2026 by the authors. Licensee MDPI, Basel, Switzerland. This article is an open access article distributed under the terms and conditions of the Creative Commons Attribution (CC BY) license.

high-performance cathode materials are indispensable to boost the comprehensive electrochemical performance of AZIBs, which still constitutes an urgent challenge in contemporary battery research [14–16].

In recent years, polyoxovanadates (POVs) have attracted considerable attention as emerging materials owing to their distinctive structural features and electrochemical characteristics [17,18]. POVs feature a tunable three-dimensional open-framework structure [19], which enables the rapid diffusion and insertion/extraction of zinc ions [20]. The rich multi-electron redox processes, combined with excellent thermal and redox stability, confer high-capacity storage and resistance to capacity fading [21,22]. These features make POVs highly suitable for overcoming the limitations of traditional AZIB cathode materials, rendering them highly competitive candidates for applications in electrochemical energy storage. To date, a range of POV-based AZIB cathode materials have been reported, such as $ZnV_6O_{16}\cdot 8H_2O$ [23], $KZnV_5O_{14}\cdot 2.5H_2O$ [24], $K_2Zn_2[V_{18}O_{28}]$ [25], and $K_{10}[V_{34}O_{82}]$ [26]. Due to the multivalent states of vanadium and the robust layered/tunnel structures capable of accommodating Zn^{2+} insertion and extraction, these materials demonstrate excellent capacity [21,22,27]. However, POV cathode materials still face certain challenges during the reaction process, such as high vanadium dissolution, low intrinsic electronic conductivity, and slow ion-transport dynamics [24]. To address these intrinsic drawbacks, diverse approaches have been developed to boost the electrochemical properties of polyoxovanadate-based cathode materials [28].

POVs exhibit a rich ability for oxidation state and structural changes, especially under electrochemical conditions, where they can undergo reversible redox reactions, forming different structures and phases [29,30]. For example, in catalytic applications, it has been demonstrated that their structure can be tuned through electrochemical redox reactions to enhance electrocatalytic activity [31]. Similarly, in general electrochemical systems, vanadium oxides enhance energy density and reaction rates through electrochemical phase transitions [32]. In AZIBs, electrochemical driving facilitates electron transfer and redox reactions, improving the ion intercalation/extraction capability of the material, as well as its stability and cycling life at high voltages [33]. For instance, Mo et al. electrochemically induced a phase transition in V_6O_{13} to obtain $V_5O_{12}\cdot 6H_2O$ cathode material, which enhanced conductivity and reduced the diffusion barrier for Zn^{2+}, thereby improving the battery's capacity and Zn-storage efficiency [34].

As research into the electrochemical behavior of POVs continues to deepen, electrochemically driven phase transitions have been proven to significantly enhance the cycling durability, energy density, and power density of batteries, thus propelling the development of aqueous zinc-ion batteries toward higher efficiency and prolonged service life. Based on these considerations, we synthesized a novel POV material, KZVO, via a simple hydrothermal method. This compound features a three-dimensional structure constructed from $\{KV_{16}O_{38}\}$ vanadium–oxygen clusters and zinc–ethylenediamine complexes. In this structure, K^+ acts as a charge-compensating ion to stabilize the structural framework, while the structurally available Zn^{2+} ions facilitate Zn^{2+} transport during battery cycling. We systematically examined the crystal structural characteristics of KZVO and the electrochemical performance of both KZVO and its phase transition product. The sufficient activation during the reaction process endows the electrode material with rapid electrochemical kinetics. Consequently, the material achieves an excellent specific capacity of 255.9 mAh g^{-1} at 0.1 A g^{-1} and retains 77.6% of its initial capacity after 2000 long-term cycles under a high current density of 4 A g^{-1}. This electrochemically induced phase transition strategy offers new insights into the application of POVs in energy storage.

2. Experimental Section

2.1. Materials

Sodium metavanadate ($NaVO_3$), lanthanum nitrate hexahydrate ($La(NO_3)_3 \cdot 6H_2O$), and ethylenediamine (en) were all obtained from Shanghai Macklin Biochemical Co., Ltd (Shanghai, China). Potassium chloride (KCl) and zinc sulfate heptahydrate ($ZnSO_4 \cdot 7H_2O$) were sourced from Shanghai Aladdin Biochemical Technology Co., Ltd (Shanghai, China). Conductive carbon black, N-methyl-2-pyrrolidone (NMP), and poly(vinylidene fluoride) (PVDF) were acquired from Dongguan Kelude Technology Co., Ltd (Dongguan, China). Zinc trifluoromethanesulfonate was purchased from Sigma-Aldrich (St. Louis, MO, USA). All reagents utilized in the tests were of analytical grade and applied directly without any further purification.

2.2. Synthesis of KZVO

KZVO was prepared via a facile hydrothermal route. In a standard synthetic process, 0.3050 g (2.50 mmol) of $NaVO_3$, 0.1726 g (2.32 mmol) of KCl, 0.0719 g (0.25 mmol) of $ZnSO_4 \cdot 7H_2O$, and 0.0525 g (0.12 mmol) of $La(NO_3)_3 \cdot 6H_2O$ were added to a 30 mL Teflon-lined reactor. Subsequently, 9 mL of deionized water was added, and the mixture was magnetically stirred at ambient temperature for 60 min. In the stirring process, 0.945 mL of ethylenediamine was added dropwise to regulate the pH value to 8.5. The as-obtained mixture was then transferred into an autoclave and hydrothermally heated at 160 °C for 72 h. After cooling down to ambient temperature naturally, the product was collected and washed repeatedly with deionized water and ethanol. Finally, the product was dried in an oven at 45 °C for 3 h to obtain the target KZVO sample (CCDC: 2547509).

2.3. Electrochemical Measurements

The as-synthesized KZVO, conductive carbon black, and poly(vinylidene fluoride) (PVDF) binder were blended at a mass ratio of 7:2:1 to prepare a uniform slurry, with N-methyl-2-pyrrolidone (NMP) as the dispersion solvent. The resulting slurry was uniformly coated onto titanium foil current collectors to form an electrode film, which was initially dried at 60 °C for 3 h and further heated at 120 °C for 12 h. The as-fabricated cathode sheet with an active mass loading of 1.0–1.3 mg cm^{-2} was used to assemble CR2032 coin cells in ambient air, with zinc metal as the anode and 3 M $Zn(CF_3SO_3)_2$ as the electrolyte. A commercial glass fiber membrane (Whatman GF/D, Cytiva, Hong Kong, China) was employed as the separator. Galvanostatic charge–discharge (GCD) tests were implemented on a NEWARE CT-4008 system within a voltage window of 0.2–1.6 V to characterize the electrochemical performance. Cyclic voltammetry (CV) and electrochemical impedance spectroscopy (EIS) were recorded on a CHI 660e electrochemical workstation (Shanghai, China) at a frequency range of 10 mHz to 100 kHz with an AC amplitude of ±5 mV. Diffusion kinetics were evaluated by galvanostatic intermittent titration technique (GITT) at 0.5 A g^{-1}, with a pulse duration of 10 min and a relaxation interval of 5 min.

2.4. Characterization

Single-crystal X-ray diffraction (XRD) data were acquired at 293 K using a Bruker Smart Apex diffractometer (Hong Kong, China), and the structure was refined using Fourier synthesis, difference Fourier synthesis, and least-squares refinement based on F^2. Powder X-ray diffraction (PXRD, Rigaku SmartLab SE, Osaka, Japan) patterns were obtained over a 2θ range of 5–50° to confirm the phase purity of the material. X-ray photoelectron spectroscopy (XPS, PHI-5000 VersaProbe III, Kanazawa, Japan) and Fourier transform infrared spectroscopy (FT-IR, Bruker Vertex 70, Ettlingen, Germany) were utilized to identify the elemental composition and chemical valence states of the vanadium–oxygen clusters

and corresponding oxides, where FT-IR spectra were collected in the wavenumber range of 400–4000 cm^{-1}. Inductively coupled plasma optical emission spectroscopy (ICP-OES, Thermo Fisher iCAP PRO, Waltham, MA, USA) was adopted to accurately quantify the elemental composition of the polyoxovanadate clusters and related oxides. Thermogravimetric analysis (TGA, Rigaku TG-DTA8122, Osaka, Japan) was carried out in a nitrogen atmosphere at a heating rate of 20 °C min^{-1} to assess the thermal stability and water content of the clusters.

3. Results and Discussion

3.1. KZVO Structural Analysis

The unit cell parameters of KZVO are listed in Table S2. This crystalline compound adopts a monoclinic system with the $P2_1/c$ space group. Its minimum asymmetric unit consists of a polyoxyanion cluster $[KV_{16}O_{38}]^{3-}$, two $[Zn(en)_2H_2O]^{2+}$ complexes, and one $[Zn(en)_{2.5}]^{2+}$ complex (Figure 1e). The molecular structure of KZVO consists of two polyoxoanions $[KV_{16}O_{38}]^{3-}$, which are formed by 16 $\{VO_5\}$ square pyramids sharing edges. Valence bond calculations indicate that the coordination number of the vanadium atom is 4.52 (Table S1) [35]. The bond lengths of V-O single bonds fall within 1.584 to 1.712 Å, whereas those of V=O double bonds range from 1.591 to 1.682 Å. Interestingly, the $[KV_{16}O_{38}]^{3-}$ cluster also contains atoms with special site-specific statistical distributions (Figure S1) [36]. At the center of the cluster, the seven-coordinated K^+ ion is directly connected to the $[V_{16}O_{38}]^{4-}$ cluster through K-O-V bonds (Figure 1a) and serves as a charge compensation ion, stabilizing the structural framework and thereby contributing to the overall stability of the material (Figure 1b). The five-coordinated Zn^{2+} ions in a square pyramidal configuration exist in two modes: (1) two Zn^{2+} ions coordinate with two en molecules, and the Zn^{2+} ions are further bridged by an en molecule, forming a chain-like structure that interacts with the cluster via electrostatic forces and hydrogen bonds (Figure 1c); (2) Zn^{2+} ions coordinate with four N atoms from two en molecules and an O ion from an H_2O molecule, while the free Zn^{2+} ions facilitate Zn^{2+} transport during battery cycling (Figure 1d). Overall, the $[KV_{16}O_{38}]^{3-}$ anion cluster, cationic complexes, en molecules, and H_2O molecules coalesce to form a three-dimensional structure that creates open three-dimensional channels for Zn^{2+} insertion and extraction, significantly reducing the migration resistance and electrostatic repulsion of Zn^{2+} within the POV's framework.

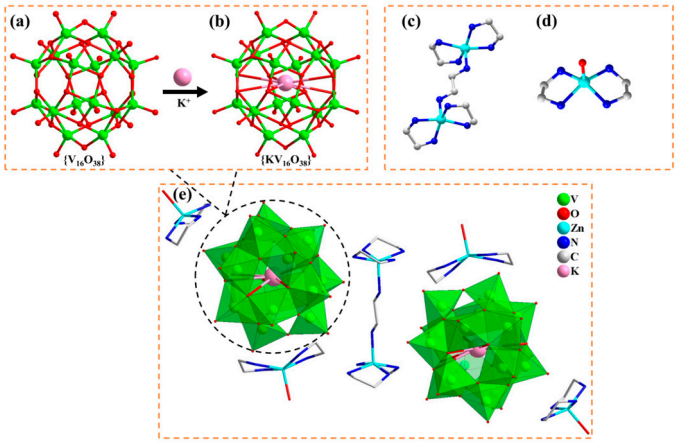


Figure 1. KZVO: (**a**) $\{V_{16}O_{38}\}$ unit ball-and-stick model diagram; (**b**) $\{K(V_{16}O_{38})\}$ unit ball-and-stick model diagram; (**c**) $[Zn(en)_5]^{4+}$ ligand unit ball-and-stick model diagram; (**d**) $[Zn(en)_2]^{2+}$ ligand unit with O atom connected model diagram; (**e**) molecular structure diagram (hydrogen atoms are omitted for ease of viewing).

Figure S2 shows the front view of KZVO along the a-axis direction. The $[KV_{16}O_{38}]^{3-}$ vanadium–oxygen clusters are arranged in a regular, periodic pattern, with adjacent vanadium–oxygen clusters interacting through electrostatic forces. These clusters, along with the $[Zn_2(en)_5]^{4+}$ and $[Zn(en)_2H_2O]^{2+}$ complexes, extend stably along the b- and c-axes, forming regular rectangular channels in the b–c plane with a channel length of approximately 22.95 Å. No apparent structural defects are present, and these channels serve as secondary pathways for Zn^{2+} transport, enhancing ion conductivity. At the same time, the K^+ ions stabilize the overall framework through K-O-V bonds, suppressing structural collapse during cycling. As observed along the b-axis (Figure S3), the $[KV_{16}O_{38}]^{3-}$ vanadium–oxygen clusters are densely packed in a columnar arrangement, closely fitting together in the a-c plane to form a continuous two-dimensional framework. The c-axis direction is characterized by narrow channels with a pore size of approximately 8.612 Å, which only supports the transport of small-radius ions, with no significant ion diffusion function. However, this direction has the highest atomic packing density and strongest compactness, serving as the core support direction for the entire crystal framework. It maintains the structural integrity of the entire crystal framework throughout repeated charge–discharge cycling, preventing material volume expansion and structural phase transitions. As shown in Figure S4, adjacent two-dimensional layers are stacked in parallel and equidistantly along the a–b plane, forming large main channels in the crystal. The interlayer spacing is uniform, with no structural defects. The channels in this direction form an interconnected ion-transport network with those in the a- and b-axis directions, serving as the main pathways for Zn^{2+} diffusion and insertion/extraction. Furthermore, large continuous voids exist between the layers, and the weak interlayer interactions provide some structural flexibility, allowing reversible modulation of interlayer spacing during ion insertion and extraction, whereas the robust intralayer bonding suppresses structural degradation upon repeated cycling.

The as-synthesized product is an unprecedented K–Zn co-doped 16-nuclear polyoxovanadate ($\{V_{16}\}$), with Zn^{2+} coordinated by ethylenediamine. To our knowledge, this specific structural configuration has not been documented in the literature. The previously documented $\{V_{16}\}$ clusters are mainly limited to Si-containing $\{V_{16}Si_4O_{46}\}$ [37], P-containing $\{V_{16}P_8O_{32}\}$ [38], and single K-doped $K_{10}[H_2V_{16}O_{38}]\cdot 13H_2O$ [39], while no analogous K–Zn co-doped $\{V_{16}\}$ structure has ever been synthesized. Moreover, only two K–Zn co-doped polyoxovanadate systems have been reported to date, both belonging to pure inorganic low-nuclearity $KZnV^{V}{}_5O_{14}\cdot 2.5H_2O$ and $K_2Zn_2[V^{V}{}_{10}O_{28}]$ with an exclusive single V^{5+} valence state. In contrast, the present $\{V_{16}\}$ material features the combination of K–Zn co-doping, ethylenediamine coordination, and a unique V^{4+}/V^{5+} mixed valence state, which is distinctly different from existing low-nuclearity counterparts. Notably, most reported $\{V_{16}\}$ polyoxovanadates merely focus on static structural characterization, without exploring their electrochemical application as AZIBs cathodes. Benefiting from the high-nuclearity framework and distinctive V^{4+}/V^{5+} mixed valence feature, this material exhibits intrinsically higher specific capacity and better rate performance than conventional low-nuclearity K–Zn co-doped polyoxovanadates. During long-term cycling, the electrode undergoes irreversible structural evolution and gradually transforms into the $Zn_3V_3O_8$ phase. The newly generated phase primarily contributes to the improved structural integrity and favorable long-cycle stability of the electrode, endowing this system with outstanding comprehensive zinc-storage performance compared with reported analogs.

Figure 2a illustrates the synthesis process of KZVO. The dried KZVO crystals were ground into powder and subjected to X-ray diffraction testing at room temperature. As shown in Figure 2b, the experimentally obtained diffraction pattern was compared with the simulated pattern, and the characteristic diffraction peaks of the synthesized KZVO crystals

closely matched those of the simulated XRD pattern, confirming the successful synthesis of a pure-phase crystalline material. To further elucidate its chemical functional groups and structural information [40], Fourier transform infrared spectroscopy was adopted to analyze the structural characteristics of the as-prepared crystalline material. As depicted in Figure 2c, the intense absorption peak at 1580 cm^{-1} is assigned to the bending vibration of O-H bonds in H_2O molecules, which verifies the existence of adsorbed surface water and lattice-bound structural water within the material [41]. The characteristic peak at 1458 cm^{-1} is ascribed to the vibrational mode associated with V(N-H), while the 971 cm^{-1} peak originates from the stretching vibration of the V-O_t (terminal oxygen) bond. The peaks at 659 cm^{-1} and 732 cm^{-1} correspond to the stretching vibrations of the V-O-V bridging oxygen bonds, and the peak at 506 cm^{-1} is related to the deformation vibration of hydroxyl groups (OH^-). This further verifies the successful preparation of high-purity KZVO. To assess the thermal stability of KZVO, TGA was performed in a nitrogen atmosphere with a heating rate of 20 °C min^{-1}, with the results shown in Figure 2d. A distinct weight loss of 3.6% was observed between 30 °C and 160 °C, ascribed to the desorption of internal water species. A gradual weight loss of 25.06% was observed over the temperature range from 160 °C to 430 °C, primarily due to the decomposition of ethylenediamine. During the subsequent heating process, the material continued to lose weight due to the thermal decomposition of the polyoxovanadate clusters. Finally, XPS was utilized to explore the elemental composition and chemical valence states of the KZVO sample. Figure 2e shows the full-survey spectrum of KZVO, in which the characteristic signal peaks of Zn 2*p*, V 2*p*, K 2*p*, O 1*s*, C 1*s*, and N 1*s* are clearly observed. This result directly verifies the existence of Zn, V, K, O, C and N elements in the as-prepared KZVO sample [42]. The high-resolution V 2*p* spectrum (Figure 2f) reveals that the V 2*p* signal consists of the V $2p_{1/2}$ and V $2p_{3/2}$ peaks at binding energies of approximately 523.1 eV and 516 eV, respectively. Peak deconvolution further confirms that vanadium exists in mixed valence states of +4 and +5 in the material. In the high-resolution Zn 2*p* spectrum (Figure 2g), the two fitted peaks at binding energies of approximately 1021.5 eV and 1043.8 eV correspond to Zn $2p_{3/2}$ and Zn $2p_{1/2}$, respectively, with the accompanying satellite peaks confirming the presence of Zn in the +2 oxidation state. The above XPS findings further validate the elemental components and chemical valence states of the as-synthesized KZVO sample, providing a solid basis for subsequent electrochemical performance studies.

3.2. Electrochemical Performance Analysis

Based on the preparation and testing procedures of the KZVO cathode and CR2032 coin cells in this study, the objective aspects that could be further optimized during the experimental process, as well as their potential minor effects on the electrochemical results, are analyzed below to further improve the research methodology and enhance data reliability. These limitations are common issues that may occur in routine laboratory testing of aqueous zinc-ion batteries and do not represent flaws in the experimental design. The details are as follows.

First, the CR2032 coin cells in this experiment were assembled in air rather than in an anhydrous and oxygen-free glovebox. This is a commonly used procedure for routine laboratory testing of aqueous zinc-ion batteries. Trace amounts of moisture and oxygen in air may have a slight influence on the battery interface. On the one hand, a small amount of moisture may be adsorbed on the surfaces of the electrode sheets and glass fiber separators, which could theoretically induce weak interfacial side reactions. On the other hand, oxygen in air may form an ultrathin passivation layer on the surface of the zinc anode, thereby slightly affecting the interfacial impedance. However, in this study, the above effects were minimized by completing the assembly rapidly, with each assembly process controlled

within 10 min, and by maintaining the laboratory temperature and humidity at 25 ± 2 °C and 50 ± 5% relative humidity. No obvious interfacial side reactions induced by ambient moisture and oxygen, as well as abnormal capacity decay, were detected in the test process, indicating that the influence of this assembly method on electrochemical performance was within a controllable range. In future work, assembling the cells in a glovebox could further eliminate potential interference from air components and improve data stability. Second, the mass loading of the cathode active material in this study was controlled within the range of 1.0–1.3 mg cm^{-2}. This loading range is consistent with the routine laboratory testing standards for cathode materials in aqueous zinc-ion batteries, and the fluctuation of 0.3 mg cm^{-2} is a reasonable deviation associated with manual coating. Such a slight variation may have a minor influence on the electrochemical performance. When the mass loading is relatively high, the electrode thickness slightly increases, which may slightly increase the solid-state diffusion resistance of Zn^{2+} and lead to a weak decrease in rate performance at high current densities. When the mass loading is relatively low, the polarization effect is relatively weaker, and the specific capacity may be slightly overestimated. To reduce the influence of this deviation, multiple parallel experiments were conducted, and cathode sheets with an active material loading of 1.0 mg cm^{-2} were selected for testing. This mitigated the interference from mass-loading fluctuations greatly, enabling the results to reliably reflect the intrinsic electrochemical properties of the material. In future work, the coating process could be further optimized, for example, by using an automatic coating machine, to narrow the fluctuation range of mass loading and improve data consistency. Third, the key processing parameters in this experiment were clearly defined, including the material ratio of KZVO, conductive carbon black, and PVDF at 7:2:1; the drying conditions of 60 °C for 3 h followed by 120 °C for 12 h; and the electrolyte system of 3 M $Zn(CF_3SO_3)_2$. These basic parameters provided a good foundation for the experimental reproducibility. However, some detailed parameters, such as the uniformity of manually coated electrode sheets and the vacuum storage time of the electrode sheets after drying, were not further standardized with higher precision. In future work, the experimental procedure could be further standardized by using an automatic coating machine to control electrode thickness and uniformity and by storing the dried electrode sheets under vacuum. These measures are expected to further enhance the reproducibility and comparability of subsequent experimental data.

In summary, the preparation and testing methods used in this study are consistent with the conventional research practices in this field. The above-mentioned potential areas for methodological optimization are common issues that can be improved in laboratory testing, and they do not affect the reliability of the experimental data or the scientific validity of the research conclusions.

Figure 3a shows the configuration of the rechargeable aqueous KZVO/Zn battery, with KZVO as the cathode and Zn metal as the anode. To investigate the electrochemical properties of KZVO as a cathode candidate for aqueous zinc-ion batteries, KZVO/Zn coin-type cells were fabricated under ambient air, followed by a series of electrochemical measurements. Figure 3b presents the cyclic voltammetry curves of the KZVO cathode for the initial three cycles, which were tested at a scan rate of 0.1 mV s^{-1} within the voltage window of 0.2–1.6 V (vs. Zn^{2+}/Zn). Two pairs of redox peaks appear at 0.49/0.68 V and 0.96/1.12 V, suggesting that the energy storage process follows a multistep Zn^{2+} insertion/extraction mechanism [43]. The additional oxidation peak in the first cycle is attributed to the incomplete extraction of some of the inserted Zn^{2+}, while the noticeable shift in the first CV curve reflects the activation process of the electrode. The similar shapes of the latter two CV curves demonstrate the excellent reversibility of Zn^{2+} insertion/extraction. The rate performance was assessed by stepwise elevating the current density ranging from 0.5 to

5.0 A g^{-1} (Figure 3c). The reversible discharge specific capacities of cathode material at 0.5, 1.0, 2.0, 4.0, and 5.0 A g^{-1} were 125.3, 208.6, 188.8, 147.3, and 123.1 mAh g^{-1}, respectively. Even at a high current density of 2.0 A g^{-1}, the reversible capacity still maintains 71.8% of the baseline value, with the specific capacity at 0.5 A g^{-1} taken as the reference standard.

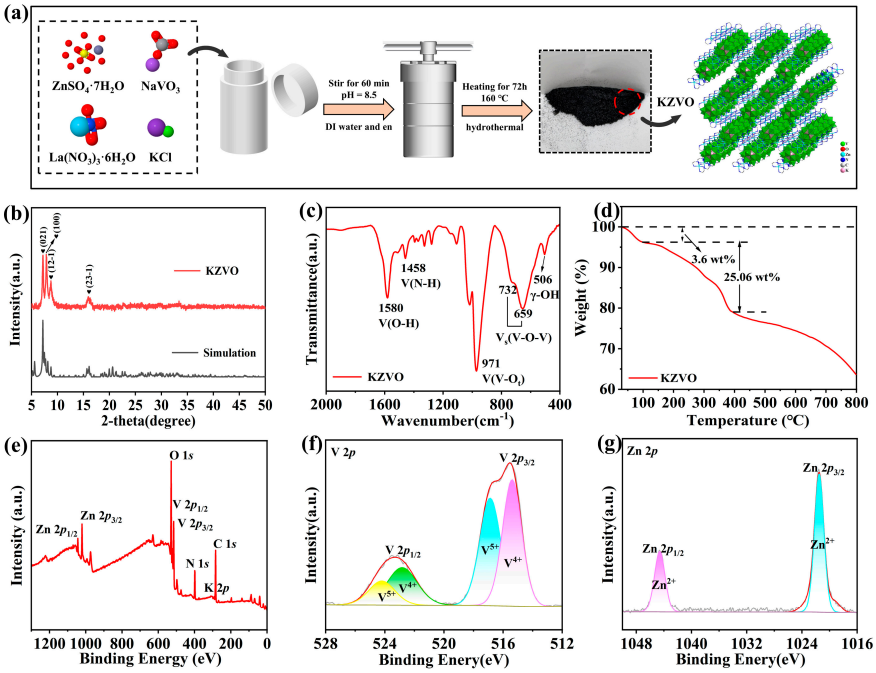


Figure 2. Material synthesis and characterization of KZVO: (**a**) schematic diagram of the synthesis process; (**b**) XRD pattern; (**c**) FT-IR spectrum; (**d**) thermogravimetric curve; (**e**) full XPS survey spectrum; high-resolution XPS spectra of (**f**) V 2*p* and (**g**) Zn 2*p*.

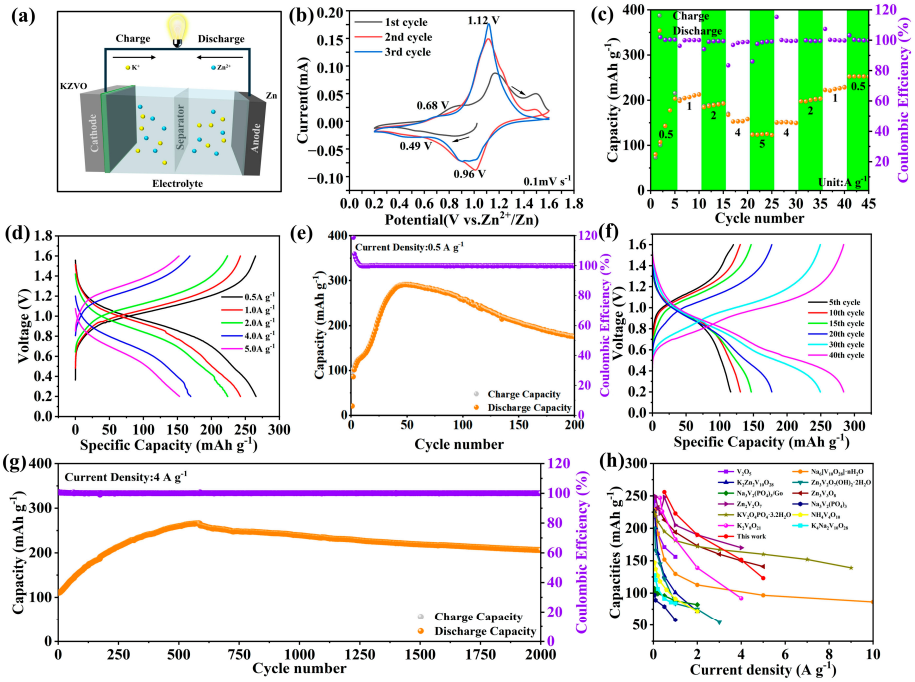


Figure 3. Electrochemical performance of KZVO: (**a**) illustration of charge/discharge process for KZVO/Zn aqueous rechargeable battery; (**b**) CV curves of the initial three cycles at a scan rate of 0.1 mV s^{-1} (arrow direction is the current scanning direction); (**c**,**d**) rate performance and corresponding galvanostatic charge–discharge profiles; (**e**,**f**) cycling performance at 0.5 A g^{-1} and charge–discharge curves at selected cycles; (**g**) long-term cycling stability at 4 A g^{-1}; (**h**) rate-performance comparisons with reported materials for AZIBs.

When the current density switched back from 5.0 to 0.5 A g^{-1}, the specific capacity quickly rebounded to 255.9 mAh g^{-1}, while the coulombic efficiency remained at 100% throughout the test. As shown in Figure 3h, we selected the maximum discharge capacities obtained from cycling at different scan rates to compare the rate performance with that of reported materials. The results demonstrate that the performance of this material is superior to that of other polyoxovanadate materials [24]. This result confirms that the cathode material possesses efficient ion-transport pathways, which can effectively alleviate the adverse effects of polarization at high current densities. Figure 3d shows the GCD curves corresponding to the rate-performance test. The highly consistent curve profiles at different current densities demonstrate that the cathode material maintains a stable charge-transfer mechanism during the charge/discharge process, reflecting its excellent structural stability and charge-transfer kinetics. The long-term cycling measurement at 0.5 A g^{-1} (Figure 3e) reveals that the discharge specific capacity reaches 291.4 mAh g^{-1} at the 47th cycle and retains 174.6 mAh g^{-1} after 200 cycles, with a coulombic efficiency of 99.9%. For the charge/discharge curves at selected cycles under this current density (Figure 3f), the relatively low coulombic efficiency in the initial stage may be due to SEI-layer formation, side reactions, and incomplete extraction of some of the Zn^{2+} [44]. The subsequent curves show significant overlap, consistent with the CV results, further confirming the battery's stability during the reaction process. To assess the long-term cycling stability of the cathode material, a 2000-cycle test was conducted at 4.0 A g^{-1} following the rate-performance measurements. As shown in Figure 3g, the electrode material accumulated lattice stress during repeated charge/discharge cycles at stepped current densities [31]. When the current density was directly switched from a low value to 4.0 A g^{-1} for prolonged high-rate cycling, this abrupt change imposed a strong non-steady-state impact on the electrode system, leading to rapid capacity decay [45]. The capacity then gradually increased, which is attributed to the electrochemically induced phase transition in the structure, with activation of the interfacial active sites enhancing the interfacial storage of Zn^{2+} [46]. The optimal specific capacity of 265.56 mAh g^{-1} was achieved at the 584th cycle. After 2000 consecutive cycles, the reversible discharge capacity still remained at 206.45 mAh g^{-1}, delivering a capacity retention rate of 77.6%.

To further explore the electrochemical reaction kinetics and pseudocapacitive behavior of the cathode material, cyclic voltammetry tests were carried out at scan rates ranging from 0.1 to 1.6 mV s^{-1} [47]. As illustrated in Figure 4a, with the increase in scan rate, the oxidation peaks gradually shift toward higher potentials, while the reduction peaks move to lower potential positions. Additionally, both peak intensity and width increase. This behavior reflects slight polarization of the electrode at different scan rates; however, the overall shape of the CV curves remains similar, indicating that the cathode material possesses good structural stability during Zn^{2+} storage. In the analysis of CV profiles, all redox peaks were determined following a consistent data picking rule. For well-isolated Peak 1, Peak 2 and Peak 4, characteristic potential and current values were collected via the baseline tangent approach. As for Peak 3 showing obvious overlapping features across the tested scan rates, no artificial peak fitting or deconvolution was performed. Instead, the maximum current intensity on the overall peak envelope was directly adopted throughout all rates. This consistent picking protocol avoids subjective deviation from manual peak splitting and ensures the validity of peak current data as well as the robustness of the subsequent b-value kinetic calculation. To investigate the kinetic mechanism of Zn^{2+} storage in the cathode material, we analyze the CV data using the power-law relationship

derived from classical cyclic voltammetry electrochemical kinetics, which has been widely employed for quantitative analysis of electrode reaction dynamics [43]:

$$i = av^b, \tag{1}$$

where i represents the peak current (A), v represents the scan rate (mV s^{-1}), and a and b are adjustable parameters. According to the Randles–Sevcik equation [48], the theoretical b value is determined as 0.5 for a purely diffusion-controlled electrochemical process, while the b value equals 1 for a typical pseudocapacitive-controlled process dominated by surface faradaic reactions. Accordingly, a b value close to 0.5 suggests that the capacity contribution is primarily governed by Zn^{2+} diffusion behavior within the electrode bulk, and a b value approaching 1 indicates that the capacity mainly originates from surface-controlled capacitive processes [49]. In practice, the electrochemical behavior of aqueous zinc-ion battery electrodes typically involves contributions from both mechanisms. To further quantify the kinetic characteristics, a logarithmic transformation was performed on both sides of Equation (1), converting the nonlinear power-law relationship into a linear correlation:

$$\log(i) = \log(a) + b\log(v), \tag{2}$$

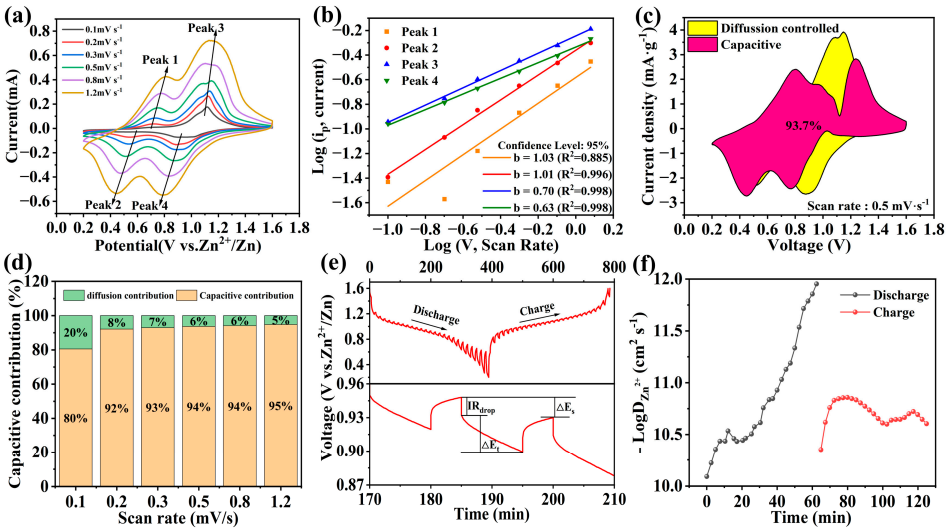


Figure 4. Electrochemical kinetic analysis of KZVO: (**a**) CV curves at various scan rates; (**b**) fitting plot of log(i) versus log(v); (**c**) pseudocapacitive contribution ratio at the scan rate of 0.5 mV s^{-1}; (**d**) pseudocapacitive contribution ratios at different scan rates; (**e**) schematic illustration of the GITT test procedure (bottom) and the time–voltage profile (top); (**f**) Zn^{2+} diffusion coefficients during cycling.

The kinetic characteristic index b can then be determined as the slope of the linear fitting plot of log(i) versus log(v), allowing identification of the dominant kinetic mechanism. In this work, the original CV curves and baselines remain unchanged. Peak 1, Peak 2 and Peak 4 were determined via the conventional baseline tangent method without any modification. For Peak 3, which exhibits overlapping convoluted hump features without well-resolved sharp vertices, we uniformly adopted the maximum current along the peak envelope across all scan rates to ensure a consistent and physically reasonable criterion. Following this consistent peak-selection principle, the fitted b-values corresponding to the four redox peaks are 1.03, 1.01, 0.70, and 0.63, respectively, all falling within the physically meaningful range of 0.5–1.0, which reasonably reflects the mixed kinetic behavior of surface capacitive and diffusion-controlled processes. These results suggest that the charge-storage process of the cathode material is governed by both pseudocapacitive and diffusion-

controlled behaviors, with the surface capacitive effect being dominant. The theoretical capacity contributions from capacitive-controlled and diffusion-controlled processes were further quantified using the equation [50]:

$$i = k_1 v + k_2 v^{1/2}, \quad (3)$$

where k_1 and k_2 are the contribution coefficients of the two respective mechanisms. As shown in Figure 4c, at a scan rate of 0.5 mV s^{-1}, the pseudocapacitive contribution accounts for up to 93.7% of the total capacity, corresponding to the pink region in the figure. In addition, the pseudocapacitive contribution ratios at different scan rates from 0.1 to 1.2 mV s^{-1} were calculated. When the scan rates were 0.1, 0.2, 0.3, 0.5, 0.8, and 1.2 mV s^{-1}, the corresponding pseudocapacitive contributions were 80.5%, 92.1%, 92.9%, 93.7%, 94.1%, and 94.8%, respectively (Figure 4d). It can be seen that the pseudocapacitive contribution gradually increases with increasing scan rate. These results indicate that the capacitive charge-storage mechanism promotes substantial accumulation and rapid storage of Zn^{2+} at the surface of the electrode, thus ensuring efficient Zn^{2+} insertion/extraction during charge and discharge. Meanwhile, the cathode material follows an insertion-type pseudocapacitive mechanism, with the high pseudocapacitive contribution providing robust kinetic fundamentals for its outstanding rate performance and superior long-cycle stability. To further investigate the diffusion kinetics of Zn^{2+}, GITT measurements were systematically conducted. The test was performed during the stable stage of the third cycle of the battery at a constant current density of 0.05 mAh g^{-1}. Specifically, the battery was first discharged (charged) at a constant current density of this value for 10 min and then kept static for 5 min to allow the voltage to stabilize and reach the equilibrium state [26]. This charge/discharge–rest sequence was repeated until the cell voltage reached the preset limit, thereby completing the full GITT test. Figure 4e presents both the enlarged view of a single charge/discharge pulse with its subsequent rest stage and the full-cycle GITT curve, which exhibits the characteristic sawtooth-like profile associated with the relaxation process. Here, ΔE_t represents the voltage change during the charge/discharge pulse, iR_{drop} refers to the voltage drop when switching between the charge/discharge and rest stages, and ΔE_s denotes the difference in steady-state voltage for a single GITT step. These parameters form the experimental basis for calculating the Zn^{2+} diffusion coefficient. Based on the data, the Zn^{2+} diffusion coefficient was calculated using the following equation:

$$DZn^{2+} = \frac{4}{\pi\tau}\left(\frac{m_B V_M}{M_B S}\right)^2 \left(\frac{\Delta E_s}{\Delta E_t}\right)^2, \quad (4)$$

In this equation, τ denotes the constant-current pulse duration, M_B stands for the mass of cathode active material, V_M represents the molar volume of the sample, m_B refers to its molar mass, and S corresponds to the contact area between the cathode electrode and electrolyte [47]. The calculated results reveal that the Zn^{2+} diffusion coefficient of the cathode material is in the order of 10^{-10}–10^{-12} cm^2 s^{-1} (Figure 4f), confirming that the cathode material exhibits excellent Zn^{2+} diffusion kinetics. This is due to the electrochemically induced formation of unique phase transition products, which provide unobstructed structural pathways for efficient Zn^{2+} insertion and extraction, significantly optimizing ion diffusion kinetics, and thus serving as a key intrinsic factor for its excellent electrochemical performance.

To further elucidate the kinetic evolution and structural stability of the KZVO/Zn cell, a set of targeted characterization tests was implemented in this work. Electrochemical impedance spectroscopy (EIS) was first carried out on the KZVO cathode before and after cycling at 4 A g^{-1} (Figure 5a), with the data fitted using an equivalent circuit containing a constant phase element (CPE), solution resistance (R_s), SEI film resistance (R_f), charge-

transfer resistance (R_{ct}), and Warburg impedance (W_s) related to Zn^{2+} diffusion [51]. It is found that after 2000 cycles, the charge-transfer resistance (R_{ct}) decreases remarkably from an initial value of 225 Ω to 52 Ω, and the overall impedance of the battery was greatly reduced. This change confirms the early-stage activation effect of the battery [52], indicating that the electrochemical activation process effectively improves the utilization efficiency of active materials and accelerates the interfacial migration and transport of Zn^{2+}. To further clarify the crystal structure evolution of KZVO and its Zn^{2+} storage mechanism during cycling, this study conducted ex situ XRD characterization on the cathode samples at 4 A g^{-1}, both during the activation process and after the reaction was completed [53]. As shown in Figure 5b, when the battery reached its maximum capacity during cycling, the XRD pattern of the electrode material changed compared with the initial pattern, indicating the formation of an electrochemically induced phase transition product. Upon further cycling until the end of the reaction, the diffraction peak positions remained highly consistent, directly confirming the excellent structural stability of the phase transition product. Phase identification further revealed that the new diffraction peaks correspond to $Zn(Zn_{0.5}V_{1.5})O_4$ (PDF#30-1494).

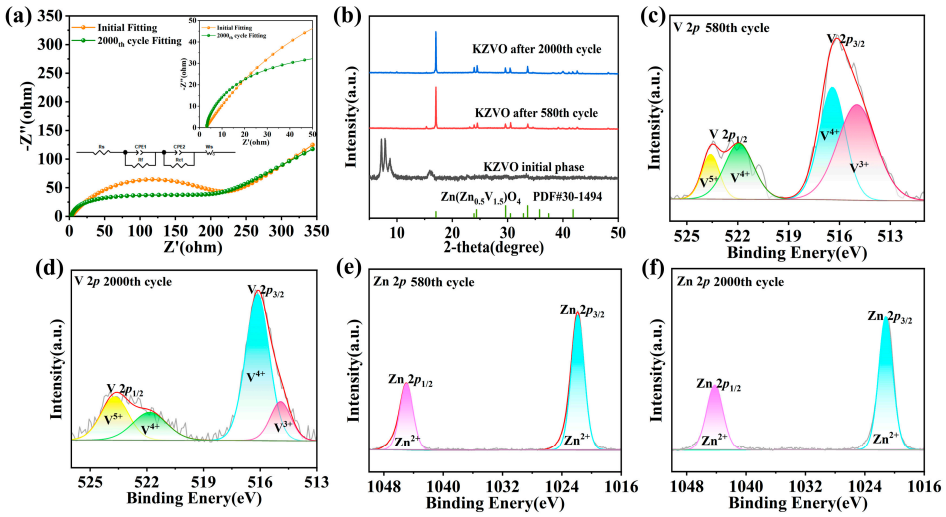


Figure 5. Structural and electrochemical characterization of KZVO at 4 A g^{-1}: (**a**) Nyquist plots of the electrode before and after cycling, the enlarged view, and the corresponding equivalent circuit; (**b**) ex situ XRD patterns at different cycles; (**c**,**d**) ex situ high-resolution V 2*p* XPS spectra; and (**e**,**f**) ex situ high-resolution Zn 2*p* XPS spectra at different cycle numbers.

Ex situ XPS characterization was further performed to investigate the valence state variation and chemical state evolution of elemental components under two different cycling conditions. As shown in Figure 5c,d, the characteristic peaks at binding energies of approximately 515.8 eV and 523.1 eV correspond to the V $2p_{3/2}$ and V $2p_{1/2}$ peaks of V^{3+}/V^{4+} and V^{5+}/V^{4+}, respectively. After cycling, the V $2p_{1/2}$ peak narrows, which is attributed to the partial oxidation of V^{4+} to V^{5+} induced by Zn^{2+} insertion, while the width of the V $2p_{3/2}$ peak remains almost unchanged, indicating a reversible redox reaction between V^{3+} and V^{4+} [54]. For the high-resolution Zn 2*p* spectra (Figure 5e,f), strong characteristic peaks are observed at 1022.3 eV (Zn $2p_{3/2}$) and 1045.1 eV (Zn $2p_{1/2}$), both before and after cycling, with no significant attenuation in signal intensity [55]. This result confirms the highly reversible Zn^{2+} storage behavior after the structural transformation. Combined with EIS and structural characterization results, it can be confirmed that KZVO undergoes in situ structural reconstruction upon continuous charge–discharge processes. The stable $Zn_3V_3O_8$ phase fully formed after 580 cycles is responsible for the highly reversible migration of zinc ions in subsequent long cycles. Meanwhile, the reversible redox reactions of vanadium

provide essential kinetic support for efficient energy storage, which serves as a crucial structural and chemical basis for the battery's excellent electrochemical performance. Based on the above discussion, it can be concluded that, in the initial stage of the electrochemical reaction, the Zn^{2+} insertion/extraction process is primarily governed by KZVO. As activation proceeds, the electrochemically induced phase transition product $Zn_3V_3O_8$ forms and participates alongside KZVO in electrochemical zinc storage, with $Zn_3V_3O_8$ playing a dominant role [56]. Therefore, we propose the reaction mechanism of KZVO as shown in Figure 6.

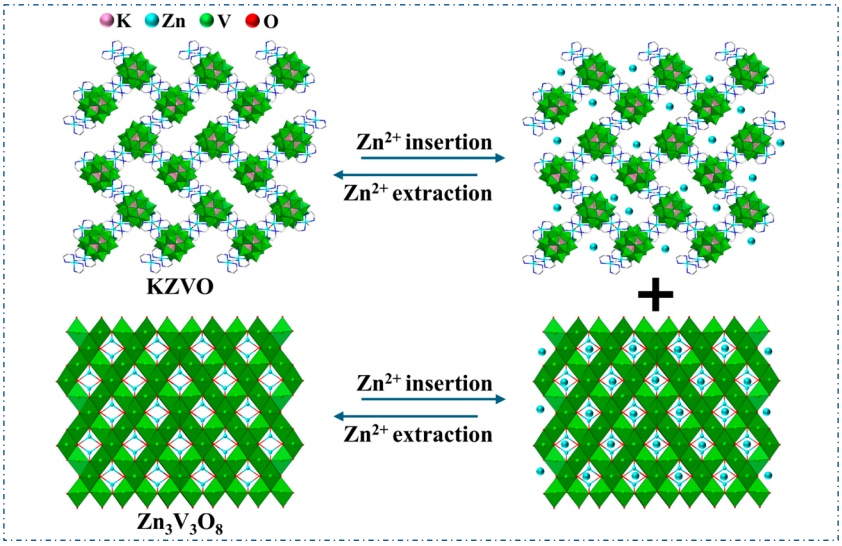


Figure 6. Schematic illustrations of the Zn^{2+}-ion storage mechanism.

4. Conclusions

In summary, this study synthesized a novel polyoxovanadate, KZVO, with a unique structure via a hydrothermal method and employed it as a high-performance Zn-storage cathode material for aqueous zinc-ion batteries. Because POVs can form different structures and phases under electrochemical conditions, they can effectively improve ion insertion/extraction capability and enhance the stability and cycling life of batteries at high current densities. As a result, the obtained KZVO material not only exhibits excellent rate performance but also achieves impressive long-term cycling stability through electrochemically induced phase transformation. Specifically, the KZVO electrode delivers a high specific capacity of 255.9 mAh g^{-1} at 0.1 A g^{-1} and retains 77.6% of its capacity after 2000 cycles at 4 A g^{-1}. This work not only provides a new high-performance POV-based cathode material but also demonstrates that the electrochemically induced phase transition can serve as a promising interfacial modification strategy. This in situ modification concept offers new insights into the development of advanced coating technologies for next-generation battery electrodes.

Supplementary Materials: The following supporting information can be downloaded at: https://www.mdpi.com/article/10.3390/coatings16050607/s1, Figure S1: The $[KV_{16}O_{38}]^{3-}$ cluster with V atoms showing special site-distribution disorder; Figure S2: 3D stacking diagram of KZVO unit cells along the a-axis; Figure S3: 3D stacking diagram of KZVO unit cells along the b-axis; Figure S4: 3D stacking diagram of KZVO unit cells along the c-axis; Table S1: The BVS of vanadium for KZVO; Table S2: Crystal structure and refinement parameters of KZVO; Table S3: The atomic coordinates ($\times 10^4$) and equivalent isotropic displacement parameters (Å $\times$ 10^3) of KZVO; Table S4: Selected bond lengths (Å) data of KZVO; Table S5: Data of selected bond angles (°) for KZVO.

Author Contributions: Conceptualization, L.J.; methodology, W.C. and L.J.; validation, W.C., F.C. and L.J.; formal analysis, W.C. and L.J.; investigation, W.C., F.C. and L.J.; resources, F.C., Y.Z., L.J. and G.W.; data curation, W.C.; writing—original draft preparation, W.C.; writing—review and editing, Y.Z., L.J. and G.W.; visualization, W.C. and L.J.; supervision, L.J. and G.W.; project administration, L.J. and G.W.; funding acquisition, Y.Z. and L.J. All authors have read and agreed to the published version of the manuscript.

Funding: This research was supported by the Zhejiang Provincial Natural Science Foundation of China under Grant No. LQN26E030006, and horizontal research project under Grant No. 251450.

Institutional Review Board Statement: Not applicable.

Informed Consent Statement: Not applicable.

Data Availability Statement: The original contributions presented in this study are included in the article and its Supplementary Materials. Further inquiries regarding the data can be directed to the corresponding authors.

Conflicts of Interest: Author Fengqiao Chen was employed by the company Hangzhou Electric Power Design Institute Co., Ltd. The remaining authors declare that the research was conducted in the absence of any commercial or financial relationships that could be construed as a potential conflict of interest.

References

1. Caldera, U.; Gulagi, A.; Jayasinghe, N.; Breyer, C. Looking island wide to overcome Sri Lanka's energy crisis while gaining independence from fossil fuel imports. *Renew. Energy* **2023**, *218*, 119261. [CrossRef]
2. Hille, E. Europe's energy crisis: Are geopolitical risks in source countries of fossil fuels accelerating the transition to renewable energy? *Energy Econ.* **2023**, *127*, 107061. [CrossRef]
3. Kayani, U.; Hasnaoui, A.; Khan, M.; Zahoor, N.; Nawaz, F. Analyzing fossil fuel commodities' return spillovers during the Russia and Ukraine crisis in the energy market. *Energy Econ.* **2024**, *135*, 107651. [CrossRef]
4. Su, C.W.; Pang, L.D.; Qin, M.; Lobonț, O.R.; Umar, M. The spillover effects among fossil fuel, renewables and carbon markets: Evidence under the dual dilemma of climate change and energy crises. *Energy* **2023**, *274*, 127304. [CrossRef]
5. Das, S.; Dutta, R.; De, S. Integrated assessment of supply risks, techno-economic and environmental factors for sustainable hybrid energy systems with emerging storage technologies: A MCDM approach. *Appl. Energy* **2025**, *399*, 126519. [CrossRef]
6. Mastoi, M.S.; Wang, D.; Zhou, X.; He, X.; Hassan, M.; Ali, A.; Rehman, A. Study of energy storage technology approaches for mitigating wind power fluctuations to enhance smart grid resilience. *Renew. Sustain. Energy Rev.* **2025**, *224*, 116072. [CrossRef]
7. Vallese, L.; Javadi, H.; Badenes, B.; Urchueguia, J.F.; Lombardo, G.; Menegazzo, D.; Ure, Z.; Cesari, S.; Bottarelli, M.; Baccega, E.; et al. A comprehensive review of thermal energy storage technologies and their applications: Creation of a database. *Renew. Sustain. Energy Rev.* **2026**, *225*, 116133. [CrossRef]
8. Wang, X.L.; Wang, D.; Zhao, Y.M. Energy storage technology innovation, performance appraisal pressure of officials and energy security: An empirical study in the context of energy transition. *Renew. Energy* **2025**, *251*, 123482. [CrossRef]
9. Dong, M.; Huang, S.M.; Yang, J.; Hou, X.H.; Chen, H.D. Two dimensional Bi_2Te_3 protective layer modified metal zinc surface to inhibit zinc dendrites in AZIBs. *J. Alloys Compd.* **2024**, *1008*, 176669. [CrossRef]
10. Li, T.T.; Guo, R.S.; Li, Y.; Meng, L.C.; Sun, X.H.; Li, F.Y.; Zhao, X.Q.; Xu, Z.K.; Peng, J.H.; An, L.Y. Long cycle performance of NC@VN/MnO cathode for AZIBs based on Mn/V relay type collaboration. *J. Energy Chem.* **2023**, *83*, 106–118. [CrossRef]
11. Wu, Q.Q.; Fu, Q.; Mu, C.H.; Ao, X.Q. Unveiling the energy storage mechanism in zinc-doped Mn_3O_4 cathode for high-performance AZIBs. *J. Alloys Compd.* **2025**, *1014*, 178843. [CrossRef]
12. Ali, A.; Mohammadi Moradian, J.; Naveed, A.; Zhang, S.; Tahir, M.H.; Shehzad, K.; Sillanpää, M. Progress in cathode materials for rechargeable Zinc-Ion batteries: From inorganic and organic systems to hybrid frameworks and biomass-derived innovations. *Prog. Mater. Sci.* **2026**, *156*, 101543. [CrossRef]
13. Li, K.X.; Li, R.; Guan, T.T.; Wang, L.; Xie, L.L.; Han, Q.; Qiu, X.J.; Cao, X.Y.; Zhu, L.M. Recent advancements in cation-intercalated vanadium oxide cathode materials for zinc-ion batteries. *Chem. Eng. J.* **2025**, *507*, 159891. [CrossRef]
14. Cheng, W.L.; Cheng, Z.Q.; Hu, Z.Z.; Hu, M.M.; Liu, G.X.; Yuan, L.F.; Fu, Y.H.; Sha, X.M.; Tu, Z.C. A fish-gelatin-modified multifunctional hydrogel with "salt-in-water" for dendrite-free flexible zinc-ion batteries. *Chem. Eng. J.* **2025**, *521*, 166945. [CrossRef]
15. Ni, H.; Fan, Z.Y.; Wang, J.W.; Wu, Y.P. Research Progress on the Mechanisms of MOF/COF and Their Derivatives in Zinc−Ion Batteries. *Energy Storage Mater.* **2025**, *77*, 104220. [CrossRef]

16. Sun, T.; Peng, H.A.; Chen, Q.; Yang, J.X.; Zhang, P.; Zhang, Y.J.; Li, S.; Qian, J.; Li, L.; Wong, S.Y.; et al. Crystalline porous organic frameworks for aqueous zinc-iodine batteries: Progress, challenges, and opportunities. *Chem. Eng. J.* **2025**, *521*, 167004. [CrossRef]
17. Fang, R.B.; Zhang, D.; Dong, J.; Feng, Y.Q.; Liu, C.P.; Yao, L.Y.; Chi, Y.N.; Hu, C.W. An open hollow polyoxovanadate cage based on {Nb(V_5)} pentagons with size-selective encapsulation properties. *Chem. Commun.* **2025**, *61*, 6182–6185. [CrossRef] [PubMed]
18. Zhang, C.H.; Wang, M.Q.; Zhao, C.H.; Wang, J.P.; Cao, Y.D.; Fan, L.L.; Liu, H.; Gao, G.G. Enhanced selective oxidation of 5-Hydroxymethylfurfural with a recyclable V_{34}@Fe_3O_4/C catalyst Enriched with Mixed-valence polyoxovanadate active centers. *Fuel* **2025**, *397*, 135439. [CrossRef]
19. Zhu, M.C.; Bai, X.; Yang, Y.L.; Zhang, A.G.; Wang, S.Y.; Sun, C.Y.; Lu, Y.; Li, B.; Liu, S.X. Nanoscale polyoxovanadate-based Mn-MOF catalyzed the cascade reaction from alcohols to imines. *J. Mol. Struct.* **2025**, *1348*, 143518. [CrossRef]
20. Wang, D.; Liu, L.L.; Jiang, J.; Chen, L.J.; Zhao, J.W. Polyoxometalate-based composite materials in electrochemistry: State-of-the-art progress and future outlook. *Nanoscale* **2020**, *12*, 5705–5718. [CrossRef]
21. Zhu, M.C.; Bai, X.; Yang, Y.L.; Zhang, A.G.; Wang, S.Y.; Wang, G.Q.; Lu, Y.; Li, B.; Liu, S.X. Kinetic-controlled synthesis of polyoxovanadate based Zn-MOFs as multifunctional catalysts for one-pot aerobic oxidation-Knoevenagel condensation reaction. *Mater. Today Chem.* **2025**, *46*, 102734. [CrossRef]
22. Hu, Y.L.; Wang, Y.Y.; Zhao, J.W.; Chen, L.J. Recent advances of polyoxometalate-based materials applied for electron-related devices. *Coord. Chem. Rev.* **2024**, *506*, 215724. [CrossRef]
23. Zhu, K.; Jiang, W.; Wang, Z.; Li, W.; Xie, W.; Yang, H.; Yang, W. Hewettite $ZnV_6O_{16}\cdot 8H_2O$ with Remarkably Stable Layers and Ultralarge Interlayer Spacing for High-Performance Aqueous Zn-Ion Batteries. *Angew. Chem. Int. Ed.* **2023**, *62*, e202213368. [CrossRef]
24. Chen, M.; He, C.; Liu, Q.; Deng, W.; Sun, C.F. A mass-producible polyoxovanadate cathode for ultrafast-kinetics zinc-ion batteries. *Inorg. Chem. Front.* **2024**, *11*, 3643–3652. [CrossRef]
25. Zhou, T.; Zhu, L.; Xie, L.; Han, Q.; Yang, X.; Cao, X.; Ma, J. New Insight on $K_2Zn_2V_{10}O_{28}$ as an Advanced Cathode for Rechargeable Aqueous Zinc-Ion Batteries. *Small* **2022**, *18*, 2107102. [CrossRef] [PubMed]
26. Yang, K.; Hu, Y.; Li, L.; Cui, L.; He, L.; Wang, S.; Zhao, J.; Song, Y.-F. First high-nuclearity mixed-valence polyoxometalate with hierarchical interconnected Zn^{2+} migration channels as an advanced cathode material in aqueous zinc-ion battery. *Nano Energy* **2020**, *74*, 104851. [CrossRef]
27. Chauhan, P.S.; Kumar, S.; Mondal, A.; Sharma, P.; Parekh, M.N.; Panwar, V.; Rao, A.M.; Misra, A. Stacked vanadium pentoxide–zinc oxide interface for optically-chargeable supercapacitors. *J. Mater. Chem. A* **2023**, *11*, 95–107. [CrossRef]
28. Xing, Z.; Xu, G.; Xie, X.; Chen, M.; Lu, B.; Zhou, J.; Liang, S. Highly reversible zinc-ion battery enabled by suppressing vanadium dissolution through inorganic Zn^{2+} conductor electrolyte. *Nano Energy* **2021**, *90*, 106621. [CrossRef]
29. Wei, S.; Wang, Y.; Chen, S.; Song, L. Structure regulation and synchrotron radiation investigation of cathode materials for aqueous Zn-ion batteries. *Chem. Sci.* **2024**, *15*, 7848–7869. [CrossRef]
30. Monakhov, K.Y.; Bensch, W.; Kögerler, P. Semimetal-functionalised polyoxovanadates. *Chem. Soc. Rev.* **2015**, *44*, 8443–8483. [CrossRef]
31. Ren, J.; Hong, P.; Ran, Y.; Wang, B.; Chen, T.; Wang, Y. High-loading and high-performance zinc ion batteries enabled by electrochemical conversion of vanadium oxide cathodes. *Electrochim. Acta* **2022**, *415*, 140265. [CrossRef]
32. Hu, P.; Hu, P.; Vu, T.D.; Li, M.; Wang, S.; Ke, Y.; Zeng, X.; Mai, L.; Long, Y. Vanadium Oxide: Phase Diagrams, Structures, Synthesis, and Applications. *Chem. Rev.* **2023**, *123*, 4353–4415. [CrossRef] [PubMed]
33. Wang, X.; Zhang, Z.; Huang, M.; Feng, J.; Xiong, S.; Xi, B. In Situ Electrochemically Activated Vanadium Oxide Cathode for Advanced Aqueous Zn-Ion Batteries. *Nano Lett.* **2022**, *22*, 119–127. [CrossRef]
34. Mo, L.; Huang, Y.; Wang, Y.; Wei, T.; Zhang, X.; Zhang, H.; Ren, Y.; Ji, D.; Li, Z.; Hu, L. Electrochemically Induced Phase Transformation in Vanadium Oxide Boosts Zn-Ion Intercalation. *ACS Nano* **2024**, *18*, 1172–1180. [CrossRef]
35. Brown, I.D.; Altermatt, D. Bond-valence parameters obtained from a systematic analysis of the Inorganic Crystal Structure Database. *Acta Crystallogr. Sect. B* **1985**, *41*, 244–247. [CrossRef]
36. Huang, M.-Q.; Chen, Y.P.; Huang, M.M.; Wei, W.J.; Sun, Y.-Q.; Lin, H.-Y. The Study on Isomer of $[V_{16}O_{38}Cl]^{4-}$ Cluster and a Mixed-Valent Polyoxovanadate Based on a New Topology. *J. Clust. Sci.* **2017**, *28*, 2795–2807. [CrossRef]
37. Shi, Y.; Zhou, T.; Di, J.Q.; Wang, W.; Ma, L.; Zhang, H.; Gao, Y. Three Si-substituted polyoxovanadates as efficient catalysts for Knoevenagel condensation and selective oxidation of styrene to benzaldehyde. *Dalton Trans.* **2022**, *51*, 3304–3313. [CrossRef]
38. Huang, L.; Yang, Y.; Yu, X.; Li, X.; Shen, Y.; Song, R.; Zhang, H. Two polyoxovanadates for visible light driven photocatalytic performance. *CrystEngComm* **2024**, *26*, 6226–6234. [CrossRef]
39. Long, D.L.; Orr, D.; Seeber, G.; Kögerler, P.; Farrugia, L.; Cronin, L. The Missing Link in Low Nuclearity Pure Polyoxovanadate Clusters: Preliminary Synthesis and Structural Analysis of a New {V_{16}} Cluster and Related Products. *J. Clust. Sci.* **2003**, *14*, 313–324. [CrossRef]

40. Zhou, T.; Xiao, H.R.; Xie, L.L.; Han, Q.; Qiu, X.J.; Xiao, Y.M.; Yang, X.L.; Zhu, L.M.; Cao, X.Y. Research on the electrochemical performance of polyoxovanadate material $K_4Na_2V_{10}O_{28}$ as a novel aqueous zinc-ion batteries cathode. *Electrochim. Acta* **2022**, *424*, 140621. [CrossRef]
41. Wang, M.; Shi, Y.; Jiang, G. 3D hierarchical $Zn_3(OH)_2V_2O_7{\cdot}2H_2O$ and $Zn_3(VO_4)_2$ microspheres: Synthesis, characterization and photoluminescence. *Mater. Res. Bull.* **2012**, *47*, 18–23. [CrossRef]
42. Zhang, M.Y.; Song, Y.; Mu, X.J.; Yang, D.; Qin, Z.M.; Guo, D.; Sun, X.Q.; Liu, X.X. Decavanadate Doped Polyaniline for Aqueous Zinc Batteries. *Small* **2022**, *18*, 2107689. [CrossRef]
43. Xiao, H.R.; Du, X.; Li, R.; Jin, H.; Xie, L.L.; Han, Q.; Qiu, X.J.; Yang, X.L.; Zhu, L.M.; Cao, X.Y. Polyoxovanadate $Li_7[V_{15}O_{36}(CO_3)]$ and its derivative γ-LiV_2O_5 as superior performance cathode materials for aqueous zinc-ion batteries. *Chem. Eng. J.* **2024**, *489*, 151312. [CrossRef]
44. Sambandam, B.; Soundharrajan, V.; Kim, S.; Alfaruqi, M.H.; Jo, J.; Kim, S.; Mathew, V.; Sun, Y.K.; Kim, J. $K_2V_6O_{16}{\cdot}2.7H_2O$ nanorod cathode: An advanced intercalation system for high energy aqueous rechargeable Zn-ion batteries. *J. Mater. Chem. A* **2018**, *6*, 15530–15539. [CrossRef]
45. Miao, L.; Jia, W.; Jiao, L. Effects of current density on Zn reversibility. *Chem. Sci.* **2024**, *15*, 18227–18238. [CrossRef]
46. Huang, R.; Wang, W.; Zhang, C.; He, P.; Han, Y.; Chen, N.; Yan, J. A bi-component polyoxometalate-derivative cathode material showed impressive electrochemical performance for the aqueous zinc-ion batteries. *Chin. Chem. Lett.* **2022**, *33*, 3955–3960. [CrossRef]
47. Xiao, H.R.; Li, R.; Zhu, L.M.; Chen, X.Z.; Xie, L.L.; Han, Q.; Qiu, X.J.; Yi, L.H.; Cao, X.Y. Mn-containing heteropolyvanadate nanoparticles as a high-performance cathode material for aqueous zinc-ion batteries. *J. Energy Storage* **2024**, *89*, 111640. [CrossRef]
48. Augustyn, V.; Come, J.; Lowe, M.A.; Kim, J.W.; Taberna, P.L.; Tolbert, S.H.; Abruña, H.D.; Simon, P.; Dunn, B. High-rate electrochemical energy storage through Li^+ intercalation pseudocapacitance. *Nat. Mater.* **2013**, *12*, 518–522. [CrossRef] [PubMed]
49. Xu, Z.M.; Zhang, W.Y.; Wang, X.Z.; Li, Y.X.; Fu, J.W.; Feng, Y.B.; Gong, W.B.; Guo, J.B.; Xue, P.; Li, Q.L. High-rate and long-life flexible aqueous rechargeable zinc-ion battery enabled by hierarchical core–shell heterostructures. *J. Mater. Chem. A* **2024**, *12*, 2172–2183. [CrossRef]
50. Li, Q.; Rui, X.; Chen, D.; Feng, Y.; Xiao, N.; Gan, L.; Zhang, Q.; Yu, Y.; Huang, S. A High-Capacity Ammonium Vanadate Cathode for Zinc-Ion Battery. *Nanomicro Lett.* **2020**, *12*, 67. [CrossRef] [PubMed]
51. Zhou, T.; Du, X.; Gao, G. Revealing the role of calcium ion intercalation of hydrated vanadium oxides for aqueous zinc-ion batteries. *J. Energy Chem.* **2024**, *95*, 9–19. [CrossRef]
52. Zhao, S.; Wang, S.; Guo, J.B.; Li, L.; Li, C.S.; Sun, Y.; Xue, P.; Wu, D.L.; Wei, L.; Wang, Y.J.; et al. Sodium-Ion and Polyaniline Co-Intercalation into Ammonium Vanadate Nanoarrays Induced Enlarged Interlayer Spacing as High-Capacity and Stable Cathodes for Flexible Aqueous Zinc-Ion Batteries. *Adv. Funct. Mater.* **2023**, *33*, 2305700. [CrossRef]
53. Cao, J.; Ou, T.Z.; Sun, Y.X.; Wu, H.Y.; Luo, D.; Yang, C.W.; Zhang, L.L.; Zhang, D.D.; Zhang, X.Y.; Qin, J.Q.; et al. High-Rate and Ultra-Stable aqueous Zinc-Ion batteries enabled by Potassium-Infused ammonium vanadate nanosheets. *J. Colloid Interface Sci.* **2024**, *665*, 32–40. [CrossRef] [PubMed]
54. Sun, R.; Xia, P.; Guo, X.; Dong, S.; Xu, F.; Zhang, Y.; Lu, S.; Zheng, Q.; Fan, H. Ternary $Zn_3V_3O_8$ superstructure and synergistic modification of separator promote high performance and stable zinc ion battery. *Chem. Eng. J.* **2024**, *486*, 150377. [CrossRef]
55. Han, Q.; Xiao, H.R.; Zhou, T.; Li, B.C.; Yang, L.; Xie, L.L.; Qiu, X.J.; Wu, X.Y.; Zhu, L.M.; Cao, X.Y. A mixed-valence polyoxometalate-based 3D inorganic framework cathode material for high-efficiency rechargeable AZIBs. *Rare Met.* **2024**, *43*, 3677–3691. [CrossRef]
56. Wu, J.; Kuang, Q.; Zhang, K.; Feng, J.; Huang, C.; Li, J.; Fan, Q.; Dong, Y.; Zhao, Y. Spinel $Zn_3V_3O_8$: A high-capacity zinc supplied cathode for aqueous Zn-ion batteries. *Energy Storage Mater.* **2021**, *41*, 297–309. [CrossRef]

Disclaimer/Publisher's Note: The statements, opinions and data contained in all publications are solely those of the individual author(s) and contributor(s) and not of MDPI and/or the editor(s). MDPI and/or the editor(s) disclaim responsibility for any injury to people or property resulting from any ideas, methods, instructions or products referred to in the content.